JET-P(95)13

Performance of Hypervapotron Beam Stopping Elements in JET

H D Falter, E Thompson.

JET Joint Undertaking, Abingdon, Oxfordshire, OX14 3EA, UK.

Preprint of a paper to be submitted for publication in
Fusion Technology

ABSTRACT

Rectangular Hypervaptron beam stopping elements made from CuCrZr have been used in the JET Beam Injectors to dissipate up to 100 MW of power. Experience over more than 10 years is outstanding with not a single failure. At the flow velocities used in the Hypervapotron elements of the JET injectors the turbulence created by the fins dominates the heat transfer and the Hypervapotron mechanism is of secondary importance. The main advantage of the Hypervapotron is the geometrical flexibility. The surface can be shaped freely as required without compromising on either heat transfer or total power handling capability. Flow velocity and flow rate can be independently adjusted to requirements. Peak power densities up to 30 MW/m^2 have been removed at a flow velocity of 7 m/s and a pressure drop of 0.25 MPa/m^2. Flow parameters were: velocity $\leq$11m/s, inlet pressure $\leq$1 MPa, inlet temperature $\leq$50°C.

1. INTRODUCTION

Hypervapotrons have been pioneered by Thompson CSF for the cooling of anodes in high power tetrodes [1]. In this technique fins are placed transverse to a forced fluid flow. The bulk fluid remains well subcooled. If the water between the fins is sufficiently stagnant, steam bubbles will grow inside the grooves and drive the warm water out. Once the steam bubble extends into the well subcooled bulk water, the bubble collapses and the colder bulk water is drawn into the groove where it re-wets the surfaces. This process allows operation with parts of the exchange surface at above the **C**ritical **H**eat **F**lux (CHF). The rate of surface temperature rise during the steam phase is reduced by heat conduction into the cold fins. This vapotron effect has been visualised by Cattadori [2] and is observed as a simultaneous event in all grooves but only at lower flow velocities.

JET has been using Hypervapotrons for all actively cooled beam dumps [3, 4, 5] of the Neutral Beam Injection system, consisting of two Injectors and a Test Bed. In total, approximately 300 beam stopping elements are in use dissipating a total power of 100 MW. The systems have been in operation for more than 10 years without a single failure.

Hypervapotrons are also being considered as heat sinks for ITER and other fusion experiments, such as TPX. At JET we have successfully used Hypervatrons as heat sinks for brazed armour tiles made from Beryllium and Carbon Fibre Composites [6, 7]. In this paper we summarise our experience with operational Hypervapotron systems and our results from various Hypervapotron tests. For convenience, we will call the Hypervapotron simply "vapotron".

2. HYPERVAPOTRONS AT JET

All the vapotrons used for the JET Neutral Beam Injectors have the same cross section (Fig.1) of 112 x 30 mm^2, but are different in length and manifolding. Two typical vapotron beam stopping elements and a complete dump assembly are shown in Fig.2. The flow velocity in all this components is of the order of 3 m/s. The critical heat flux at 3 m/s is approximately 15MW/m^2, the design peak heat flux is 10 MW/m^2. The range between 10 - 15 MW/m^2 is occasionally entered in the test bed dump. A single element has been tested up to a total power of 0.63 MW with a peak power density of 11 MW/m^2 using a flow rate of 4.7 x $10^{-3}m^3/s$ [8].

The Test Bed Dump (Fig.2b) consists of 33 vapotron elements, arranged in two plates of 15 and 18 beam stopping elements each. The total area exposed to beam power is 3.3m^2. The total flow rate is 0.1 m^3/s, the pressure drop is 0.044 MPa and the total power capability is 7 MW with a peak power density of 12 - 15 MW/m^2. The peak power per element is 0.4 MW, resulting in a temperature rise of 30°C in the cooling water. The water loop is run at a static pressure of approximately 0.3 MPa and a water temperature of 20°C. No indication of flow instability has so far been observed. This dump has been exposed to more than 75 000 pulses. The low pumping power of 4.4 kW required for the removal of 7 MW is remarkable.

An additional advantage of the vapotron concept is its geometrical flexibility. This can be demonstrated by some of the geometries used in the JET system (Fig.3): The box exit scraper (3a) protects an absolute valve between injector and torus. The opening of this valve has the shape of a racetrack and the scraper follows this shape. Additionally the angle of incidence between scraper surface and beam is reduced in the direction towards the beam centre to counterbalance the increase in power density. The fractional energy dump (Fig.3b), located close to the bending magnet, is designed to handle the fractional energy particles which have a narrow line focus. As with the box exit scraper the surface is curved to counterbalance the increase in power density. Finally the actively cooled divertor elements (Fig.3c) are wedge shaped as dictated by the toroidal geometry of the torus, and they are curved in the vertical plane to form a good divertor geometry. In the case of a vapotron all these geometrical restrains can be easily accommodated without compromising the heat removal capability.

Another important feature of the vapotron is that the component is very strong and robust with a minimum wall thickness of 3 mm. In divertor applications alignment tolerance and element bending during exposure could lead to exposed edges and to higher power densities when the angle of incidence increases due to the bending. This can be a strong effect as the JET divertor has a glancing incidence with an angle of a few degrees. To maintain the alignment the vapotron of the JET divertor design is rigidly attached onto a machined hard back made from steel. In the performance tests of these elements this was simulated by restraining the vapotron to a strongback without allowance for thermal expansion [Ref. 13].

3. MODES OF OPERATION OF HYPERVAPOTRONS

The "classical" Hypervapotron mode of operation, as described in Ref. 1 and 2, is only observed at lower flow velocities. In JET we could identify the different modes by the characteristic noise they create on the water pressure signal (Fig.4) [9]: At low flow velocity (left in Fig.4) an oscillation with a frequency of approximately 20 Hz builds up, once the surface exceeds the saturation temperature. This frequency is compatible with the model, as a simple approximation shows:

With 4 mm high fins the groove has a volume of 0.12 cm^3 per cm length. Starting with a groove full of cold water this will initially be heated up along the boundary layer with the hot wall. The hottest part of the wall is the fin root, which is closest to the exposed surface. Once this water is hot enough, steam bubbles will grow and expand into the cold bulk water stream. To heat all the water in the groove by 100°C requires 50 Joule/cm. To fill the groove with steam requires 0.4 Joule/cm for the evaporation. The heat influx in the case of Fig.4 is 5 MW/m^2 or 300 W/cm in one groove. This means that we would have a frequency of 6 Hz if all the water had to be heated before the groove can fill up with steam. Obviously only the water facing the bubble has to be hot and 20 Hz is therefore a reasonable number. From this model we expect the frequency to increase with power density and to decrease with pressure. This is consistent with the experimental observation.

The water exchange between the cold bulk flow and the grooves increases with increasing flow velocity as can be seen from the rapidly improving heat transfer with velocity in Fig.6 and vortexes are likely to develop in the grooves. Once sufficient cold bulk water is able to enter into the grooves, the steam bubbles will collapse before they can extend into the bulk water stream and the boiling becomes a local event (very much as in normal pipe flow). This is the case in the right part of Fig.4. The noise frequency is much increased. Within the frequency band of the sensor (1 kHz) no dominant frequency can be identified. This makes sense, if the boiling crisis is a local event in each individual groove and all these un-synchronised signals are contributing to the measured noise.

At higher flow velocities, when the fluid is penetrating into the grooves, we can distinguish three different heat transfer regimes, as Fig.5 shows:

- Initially the temperature rise is proportional to power density but independent of water pressure. This is the range of convective heat transfer.

- At the onset of boiling the rate of temperature rise with power is reduced. The onset of boiling is first observed for the lower water pressure. This boiling regime starts at 5.5 MW/m^2 in the case of Fig.5 with a bulk water velocity of 4 m/s. The slope in this boiling regime is the same for both water pressures. The temperature is shifted

upwards by 26°C at the higher pressure. This compares with an increase in saturation temperature of 42 °C for the higher pressure.

- Above 10 MW/m^2 we observe that the temperature becomes again independent of pressure and noise spikes appear in the water pressure signal. The amplitude of these noise spikes are marked as stars in Fig.5. After the noise has developed fully the rate of temperature rise starts to increase, however the panel reaches thermal equilibrium after a few seconds and is thermally stable. This is the range , in which the wall temperature of the fin root is above that for CHF as the numerical model suggests [10]. The noise spikes are then created from the re-wetting of the over critical wall area after the collapse of bubbles. This noise is comparable to that observed in single side heated tube sections at high power density but has roughly twice the intensity in the vapotron [Ref. 13].

To summarise, we observe a non boiling heat transfer range for low power densities, a soft boiling heat transfer regime, which is free of noise, in the medium power density range, and a noisy heat transfer regime for the highest power densities.

With increasing water velocity we observe an increase in heat transfer before the onset of boiling (Fig.6) from 0.02 MW/m^2/°C at a velocity of 0.74 m/s to 0.074 MW/m^2/°C at 8.5 m/s. This slope of heat transfer with velocity corresponds to 1.35 times that in the Dittus Boelter correlation [11]. If we regard the heat transfer as conduction through the stagnant boundary conduction layer then we must assume that the thickness of the boundary layer is smaller than that in a pipe having the same velocity and hydraulic diameter.

With the onset of boiling, we observe an improved heat transfer. This boiling heat transfer shows a further slight improvement with increasing velocity. At the highest velocity, however, the boiling heat transfer is only marginally above that before the onset of boiling. Similar conclusions have been drawn by Cattadori [Ref. 2] in his experiment with electrically heated circular Hypervapotron test sections.

In a cylindrical vapotron the water entering into the groove must flow radially towards the axis. As the surface area per unit length F~r reduces, continuity of flux would require that the velocity v increases v ~ l/r. This means that for the cylindrical geometry it is more difficult for the flow to penetrate into the grooves. The general observations are quite similar in both the plane and cylindrical vapotron however, one clear difference is that we observe in the plane vapotron a clear improvement of the heat transfer with increasing velocity in the soft boiling range in Fig.6 while no such improvement is reported for the cylindrical vapotron in this heat transfer regime (Fig.5 in ref. 2).

4. PRESSURE DROP

The dimensions of the vapotron test sections we have used for pressure drop measurements are listed in Table 1. All pressure scans show that the usual relation with the square of the bulk velocity holds. The data sets are from dedicated flow measurements made on the wide vapotrons used in the Neutral Beam Injectors (48 x 10 mm water channels) and also from flow scans on assembled test components carried out during high heat-flux tests using narrow vapotrons. Finally for a prototype divertor element, the internal pressure drop through tappings inside the vapotron body 80 and 100 mm from the ends of the vapotron was measured in order to avoid effects of the transition from the circular inlet and exit pipes to the internal rectangular cross-section.

Table 1: dimensions of the vapotrons used for pressure drop measurements

	water channel		parallel channels	cross section	d_{hydr}	internal feed diameter	F_{bulk}/F_{feed}
test section	width	height					
	[m]	[m]		[m^2]	[m]	[m]	
TBBD 2x48x10	4.80E-02	1.00E-02	2	9.60E-04	1.66E-02	4.00E-02	0.76
Calorimeter 48x10	4.80E-02	1.00E-02	1	4.80E-04	1.66E-02	2.00E-02	1.53
TBBS 48x10 hair	4.80E-02	1.00E-02	1	4.80E-04	1.66E-02	2.00E-02	1.53
narrow vapotron 19x8	1.90E-02	8.00E-03	1	1.52E-04	1.13E-02	1.30E-02	1.15
narrow vapotron 19x6	1.90E-02	6.00E-03	1	1.14E-04	9.12E-03	1.30E-02	0.86
narrow vapotron 19x3	1.90E-02	3.00E-03	1	5.70E-05	5.18E-03	1.30E-02	0.43
divertor	2.66E-02	5.57E-03	1	1.48E-04	9.21E-03	1.30E-02	1.12

4.1. Wide vapotrons with 48 x 10 mm^2 water channel

The transition from the circular feed and return pipes to the rectangular vapotron water channel can dominate the pressure drop of the test section as Fig.7 shows for three components which **all** have the **same** vapotron water channel dimensions shown in Fig.1. One element (**T**est **B**ed **B**eam **D**ump - TBBD) has rear feeds with 40 mm i.d. supplying both water channels in parallel, the second element (calorimeter) has straight feeds of 20 mm i.d. each supplying one of the two water channels, and finally the third element (scraper) has a hairpin flow with a 180° deflector at one end and a 20 mm i.d. feed at the other end. Two of the beam stopping elements (dump and scraper) are shown in Fig.2a which also shows the feed geometries. The scraper element is only 500 mm long and the pressure drop which is measured on the assembled component consisting of 3 individual elements therefore includes manifolding losses. The smallest pressure drop is for the dump element with the rear feed and is as low as 0.035 MPa/m for a flow velocity of 5 m/s. This element can easily remove 0.5 MW with a pumping

power of less than 20 Watt. Following the treatment in Wärmeatlas [12], we can express the pressure drop Δp as

$$\Delta p_v = \rho \times (\xi_{v1} \times \frac{L}{d_{hyd}} \times \frac{v_{bulk}^2}{2} + \xi_{v2} \times \frac{v_{feed}^2}{2}) \quad (1)$$

where ρ is the density, L the length of the element, d_{hyd} the hydraulic diameter of the vapotron water channel, v_{bulk} the average velocity in the vapotron, and v_{feed} the average velocity in the feed pipe. ξ_1 and ξ_2 are the friction coefficients. The subscript v stands for the various test sections (see Table 2 for nomenclature). Using continuity of flow:

$$v_{bulk} \times F_{vap} = v_{feed} \times F_{feed} \quad (2)$$

we get from equation (1):

$$\Delta p_v = \frac{\rho}{2} \times v_{bulk}^2 \times (\xi_{v1} \times \frac{L}{d_{hyd}} + \xi_{v2} \times (\frac{F_{vap}}{F_{feed}})^2) \quad (3)$$

If we assume that calorimeter and TBBD vapotron have the same coefficients $\xi_{11} = \xi_{12} = \xi_1$ and $\xi_{21} = \xi_{22} = \xi_2$ we can calculate the coefficients from a fit of pressure versus velocity ($\Delta p_v = \alpha_v \times v_v^2$)

$$\alpha_v = \frac{\rho}{2} \times (\xi_1 \times \frac{L}{d_{hyd}} + \xi_2 \times (\frac{F_{vap}}{F_{feed}})^2) \quad v = 1, 2, 3 \quad (4)$$

The flow measurement with the scraper element (TBBS) includes manifolding losses and a pressure drop due to the 180° deflection for the hair pin flow and will therefore yield a larger coefficient ξ_2. Equation 4 defines all three friction factors ξ_1, ξ_2, and ξ_{32}. Using this analysis we find that 62% of the measured pressure drop is inside the vapotron in the case of the dump element (TBBD) and 29% and 21% in the case of calorimeter and scraper. This shows that the actual pressure drop per metre length can easily be dominated by feed losses. The assumptions that ξ_1 is the same for all three elements is reasonable since the vapotron body is the same for all three elements. The assumption $\xi_{12}=\xi_{22}$ is arbitrary because the feed geometries are different and is only used for convenience.

4.2. Narrow vapotrons

With the exception of the divertor element these flow scans are of lower quality than those for the wide vapotrons and may include a pressure loss component from the supply pipes. Data from narrow vapotrons, tested as part of the development of a possible JET divertor, are shown in Fig.8. The narrow elements were 485 mm long and were normally tested in pairs. All narrow elements in Fig.8 have 4 mm high fins with 3 mm fin width and fin spacing. The pressure drop measurement is taken over two elements in series for a water channel cross section of 19x8 and 19x6 mm^2. The test section with the narrow water channel was measured in a single element and we plot twice the measured pressure drop in Fig.8. Also included in Fig.8 is the pressure drop for a divertor element. This element is 870 mm long and tapered in width with the internal width of the water channel increasing linearly from 20.7 mm at one end to 30.3 mm at the other end. The height of the water channel varies from 6.5 mm at the narrow end to 4.5 mm at the wide end in order to maintain constant cross sectional area along the length of the element. For these long divertor element the internal pressure drop was measured. The average hydraulic diameter and velocity shown in Table 1 is averaged over the expression:

$$\int_0^1 v^2(z) \div d_{hyd}(z) x dz = (v^2 \div d_{hyd})avg \quad x1$$

The pressure drop in all 4 elements is quite similar and shows little influence of the ratio F_{bulk}/F_{feed} in Table 1. This indicates that

- the hydraulic diameter in (3) is not the proper scaling parameter. The variation in hydraulic diameter in the narrow vapotrons does not cause a corresponding variation in pressure drop and the difference in pressure drop between wide and narrow vapotrons is larger than expected from the change in hydraulic diameter.

- Feed losses are less important in the case of the narrow vapotron. The pressure drop in the bulk section appears to be dominant and the variation in F_{bulk}/F_{feed} has a minor influence.

The higher pressure drop in the narrow vapotron is surprising and additional data are required to determine how the pressure drop scales with the width and the height of the water channel. In order to derive a guide-line value for the pressure drop in these elements we assume that equation 3 is also meaningful for the **narrow** vapotron channel and obtain the pressure drop per metre length in Pa/m for the vapotron body as

$$\Delta p \div L = 1388 \times v_{bulk}^2 \qquad (5)$$

for a water channel of 48 mm width and

$$\Delta p \div L = 5038 \times v_{bulk}^2 \qquad (6)$$

for 19 mm wide elements (v in m/s). Equation (6) is taken as the average from the internal pressure scan with the divertor element and the scan from the vapotron with the smallest water channel (19x3 mm^2) which has the smallest losses from the feed.

5. MAXIMUM HEAT FLUX WITHOUT BURNOUT

Normally we do not test vapotrons to destruction. The "critical heat flux" becomes the point, at which the experimentalist decided to stop increasing the power density and hence our definition of the critical heat flux (CHF) (which is better called "maximum heat flux before burnout") depends on the risk the experimentator is prepared to take! In Fig.6 for example the scan at 0.74 m/s stops at a wall temperature of 200°C above the water temperature, while the scan at 4.2 m/s continues up to a wall temperature of 400°C above the water temperature. In other cases the power scan is terminated if the temperature appears not to achieve an equilibrium value. If we chose to define the end points of our scans as maximum heat flux without burnout (which is a **lower** limit of CHF), we obtain an increase in this maximum heat flux with the 0.6th power of bulk flow velocity (Fig.9). The data point (black circle) at 11 m/s was taken in a comparative test with an adjacent swirl tube section [13]. In this test, the swirl tube was close to CHF and tripped a temperature interlock. This limited the peak power density and the actual limit of the vapotron at this flow velocity has not been measured.

From Fig.9 we can derive a critical heat flux h_{crit} in MW/m^2 purely as a function of flow velocity in m/s.

$$h_{crit} > 7.8 \times v^{0.6}$$

for water at room temperature. Within the accuracy of the measurement we do not observe an influence over a limited range of fin geometry or water pressure.

All the measurements of Fig.9 (except the one with 8 mm fins) were carried out using the arrangement shown in Fig.10: Two test sections were installed side by side with the water flowing either in parallel or in the series connection shown in Fig.10. In the case of series connection we use data from the upstream test section for Fig.9. The test sections are exposed to beam power over a height of 200 mm ad the profile of the impinging power is measured to be Gaussian with an e-folding length of typically 120 mm. The average power density is 80-85% of the peak power density.

The influence of water temperature or subcooling is difficult to quantify with our particular experimental set-up and only limited data are available. Since our water loop passes through a heat exchanger at room temperature and has no heater, we have to bypass the heat exchanger and let the loop warm up mainly from the dissipation of the circulation pump in order to vary the inlet temperature. This procedure is tedious and not easily controllable. Nevertheless some data are shown in Fig.11 for power scans at average pressures of 7.8 and 3.7 bar and at water inlet temperatures of 15, 40 and 50°C. Up to approximately 15 MW/m^2 we observe hardly any variation in the heat transfer with either pressure or temperature. Above 15 MW/m^2 the temperature rise is significantly increased when the inlet temperature rises from 40 °C to 50 °C and the maximum heat flux is reduced by approximately 4 MW/m^2 while an increase in inlet temperature from 15 to 40 °C appears not to influence the heat transfer. The actual water exit temperature T_{exit} of the test section in Figs.11 and 9 can be derived from $T_{exit} = T_{in} + 3.4 \frac{^{o}C\ m^3/h}{MW/m^2} \times p_{max} / flow$. For the flows in Fig.11 the exit water temperature at 24 MW/m^2 is 40 °C above the inlet temperature and a degradation in heat transfer seems to occur when the exit temperature approaches 90 °C. This limit appears to be a temperature limit, as it is observed for both water pressures. A possible explanation is that initially the increase in viscosity with temperature improves the flow into the grooves and with it the heat transfer and we observe that the surface temperatures are actually slightly lower for the higher inlet temperature. If the water temperature gets too high the heat transfer starts to suffer. An extrapolation from these data to operation at considerably higher pressures or water temperatures is not advisable.

In a recent experiment, [7], a vapotron operating with a flow velocity of 7 m/s and clad with 8 mm thick unidirectional CFC tiles was exposed to a power density of 30 MW/m^2 for pulse lengths of up to 10 s without burnout. This heat flux is well above the fitted curve in Fig.9 and it is not clear if the armour tiles or if additional turbulence due to the restricted cooling water inlet geometry is responsible for an increased heat transfer. It could be true that the hot armour tile by simply obstructing the view of the front copper surface normally used to monitor the approach to burnout, led us to continue above the (arbitrary) power density where we would have normally stopped the test. Radiation loss is approximately 0.8 MW/m^2 and does not account for the difference. If the incident power density is increased such that burnout is approached in a vapotron, the measured average surface temperature rise is not very fast (125 °C /s) as Fig. 12 shows. The likely reason is that the lower part of the fins are still cooled and continue to act as a heat sink when cooling at the fin root is reduced due to local burnout.

6. MECHANICAL BENDING DURING EXPOSURE

The bending of the element is measured as the deflection of the lower end of the element (Fig.10). This deflection is plotted against the temperature measured with a thermocouple 2 mm below the exposed surface and against power density (Fig.13). For temperatures up to 300 °C, bending is proportional to temperature resulting in a bend radius R_{bend}= 9.6 10^5 [mm °C]/T_{TC}, with T_{TC} being the temperature in the side wall three millimetre below the exposed surface, (measured with a percussion welded thermocouple). Above 300 °C or 12 MW/m^2 the bending saturates. The saturation in bending indicates the onset of plastic deformation and sets an independent limit for routine exposure.

7. CONCLUSION

Hypervapotrons have been extremely successful as heat sinks in the JET beam injectors providing high reliability and safety. The vapotrons at JET are routinely running with a safety factor of 1.3 and it is remarkable that we had no failure over more than 10 years of operation.

Hypervapotrons give considerable freedom in the design of the components: The contour of the exposed surface can be adjusted to the impinging power density and the water channel cross section can be adjusted to the required flow rate thus allowing flow velocity and flow rate to be optimised independently. The pumping power can be remarkably low but the transition from the circular feed pipe to the rectangular vapotron channel needs care in the design since this can dominate the pressure loss.

Over the range of flow velocities we have used, the Hypervapotron can be considered as simply a finned surface where the fin provides an increased heat exchange area in addition to acting as turbulence promoter (vortex flow). The fins also provides additional thermal mass which increases the time taken for a complete burnout to occur. The originally conceived Hypervapotron effect is of secondary importance, but could be useful in the case of accidental loss of pumping power.

REFERENCES

[1] Beutheret, C. Transfert de flux superieur a 1 kW/cm^2 par double changement de phase entre une paroi non isotherme et une liquide en convection forces, Proc. Int. Heat Transfer Conf., Paris 1970.

[2] Cattadori, G et al., Hypervapotron Technique in Subcooled Flow Boiling CHF, Experimental Thermal and Fluid Science 1993; 7:230-240.

[3] G Düsing et al, "Neutral Beam Injection System", Fusion Technology, Vol. 11, PP 163-202, Jan 1987.

[4] R Haange, "Design of Calorimeter and Ion Dump for JET Neutral Injection Line", Proc. 9thSymp. Engineering Problems of Fusion Research, Chicago, Illinois, October 26-29, 1991, p. 1352, Institute of Electrical and Electronics Engineers (1981).

[5] H D Falter et al, "The Neutral Beam Test Bed Facility and First Results", Proc of the 13th Symp on Fus Techn., Varese, 24-28 Sept., (1984) p 571, Pergamon Press, ISBN 0 08 0325599.

[6] H D Falter et al, "Testing of plasma facing materials for divertors in the JET neutral beam test bed. "High Heat Flux Engineering II, Ali M, Khounsary, Editor, Proc. SPIE 1997, p. 170 (1993).

[7] H D Falter, "Vapotron as heat sink for flat high conductivity unidirectional CFC tiles", Fusion Technology, this issue.

[8] R Tivey et. al., Testing of beam stopping elements using Hypervapotron Cooling, Proc. 12th Symp. on Fusion Engineering (SOFE), Monterey, USA, 12-16 October 1987. Also available as Report JET-P(87)52, pp. 50-53

[9] H D Falter et al, Power loading tests of the JET pumped divertor plates, Proceedings of the 16th Symp on Fus Techn, London U.K., 3-7 Sept, 1990, ISBN 0 444 88508 0, Elsevier Science Publishers BV. 1991

[10] C Baxi et al, A Model for Analytical Performance Prediction of Hypervapotron, JET-P(92)56

[11] W M Rosenhow, et al, editors, "Handbook of Heat Transfer Fundamentals", McGraw-Hill Book Co, New York, 1983

[12] VDI-Wärmeatlas, Berechnungsblätter für den Wärmeübergang, VDI-Verlag Gmbh, Düsseldorf, Germany, ISBN 3-18-400415-5

[13] H D Falter et al, "Thermal test results of the JET divertor plates," High Heat Flux Engineering, Ali M. Khounsary, Editor, Proc. SPIE 1739, p162, (1992)

Table 2: Nomenclature	
d_{hyd}	hydraulic diameter
F_{feed}	cross sectional area in the feed pipe
F_{bulk}	cross sectional area in the water channel
H_{crit}	critical heat flux
P_{max}	peak power density
v_{feed}	average velocity in the feed pipe
v_{bulk}	average velocity in the water channel
α	fitting parameter in $\Delta p=\alpha v^2$
ξ_1	friction factor in the vapotron body
ξ_2	friction factors of the feed/return pipe and manifold

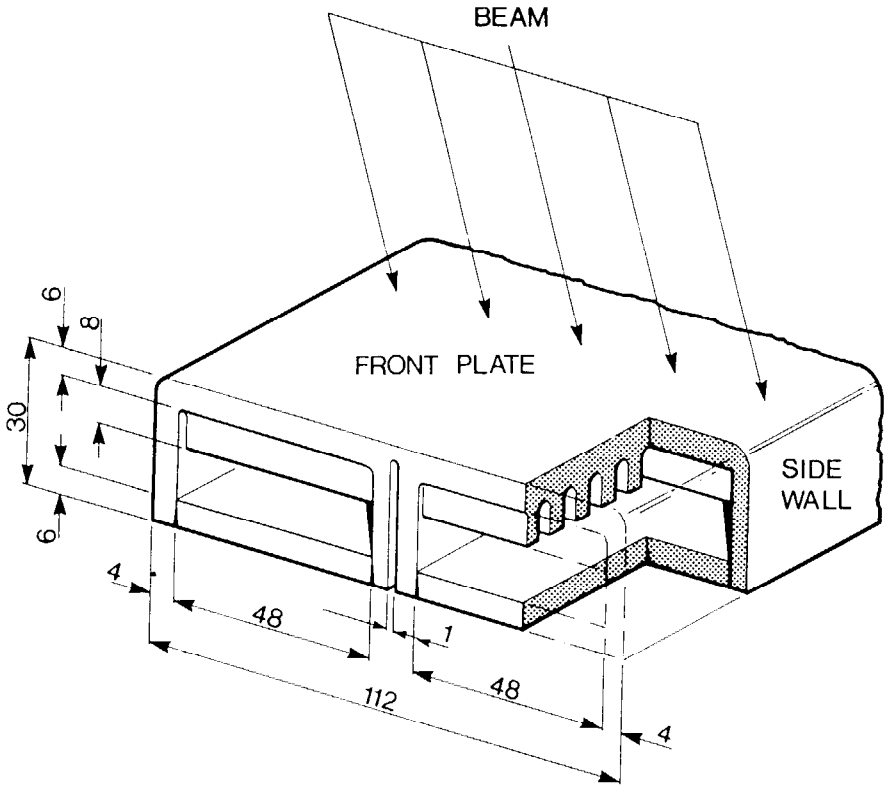

Fig.1: Dimensions of the standard JET flat Hypervapotron.

Test bed dump element

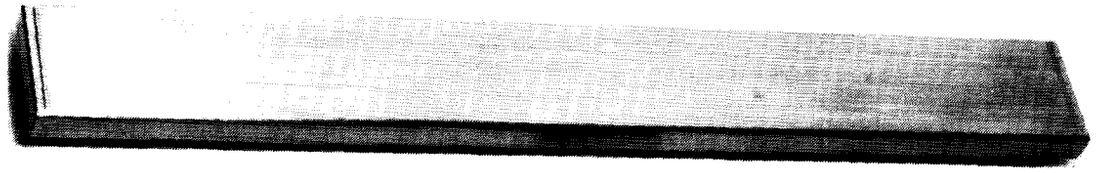

Feed details dump element

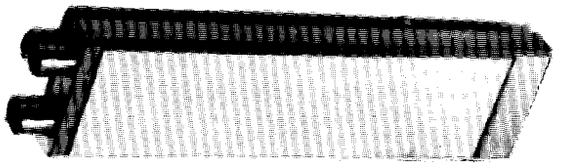

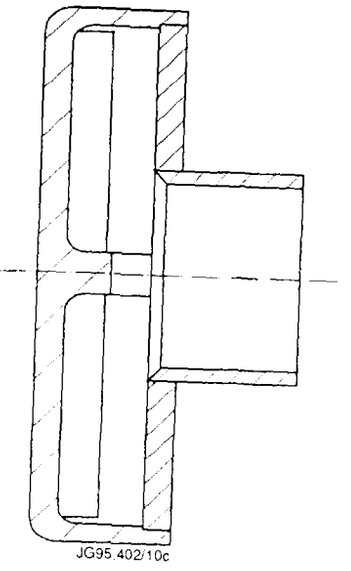

Test bed scraper beam stopping element–water feed details

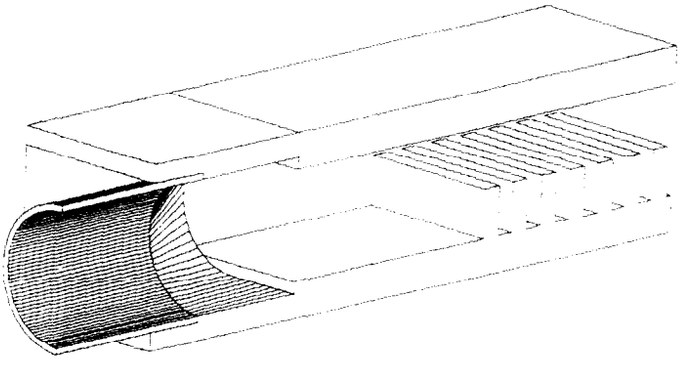

JET calorimeter vapotron–water feed details

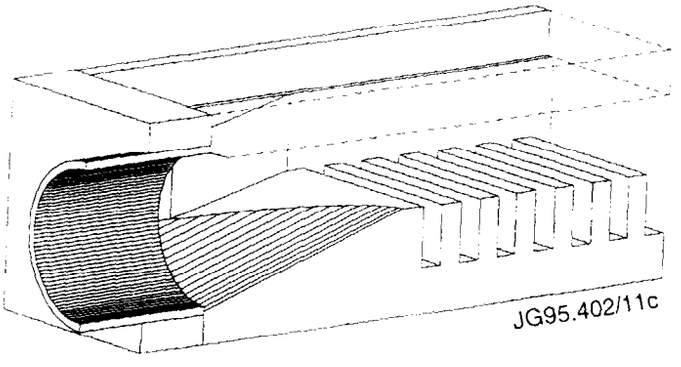

Fig.2a: Hypervapotron beam stoppimg elements as used in the JET Test Bed beam bump, the calorimeter, and the Test Bed box scraper (TBBS). The length is 1000 and 500 mm. Feed diameter is 40 and 20 mm id. The scraper element has a hair pin flow with an internally closed loop.

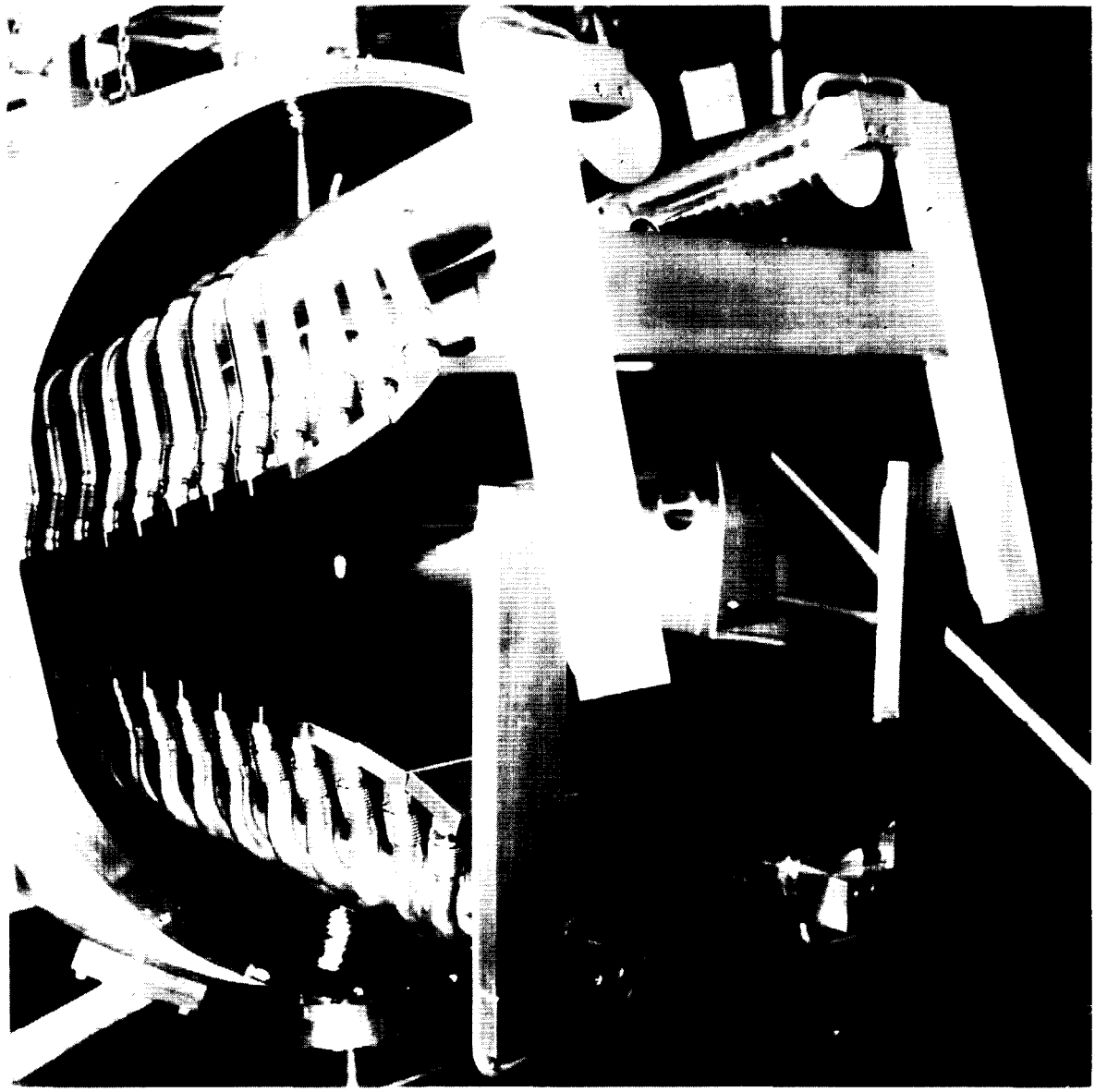

Fig.2b: JET Test Bed Beam Dump. 33 beam stopping elements are arranged on two plates.

Fig.3a: Box Exit Scraper. The Hypervapotrons at the top and bottom are curved in two planes. Feed and return is in the centre.

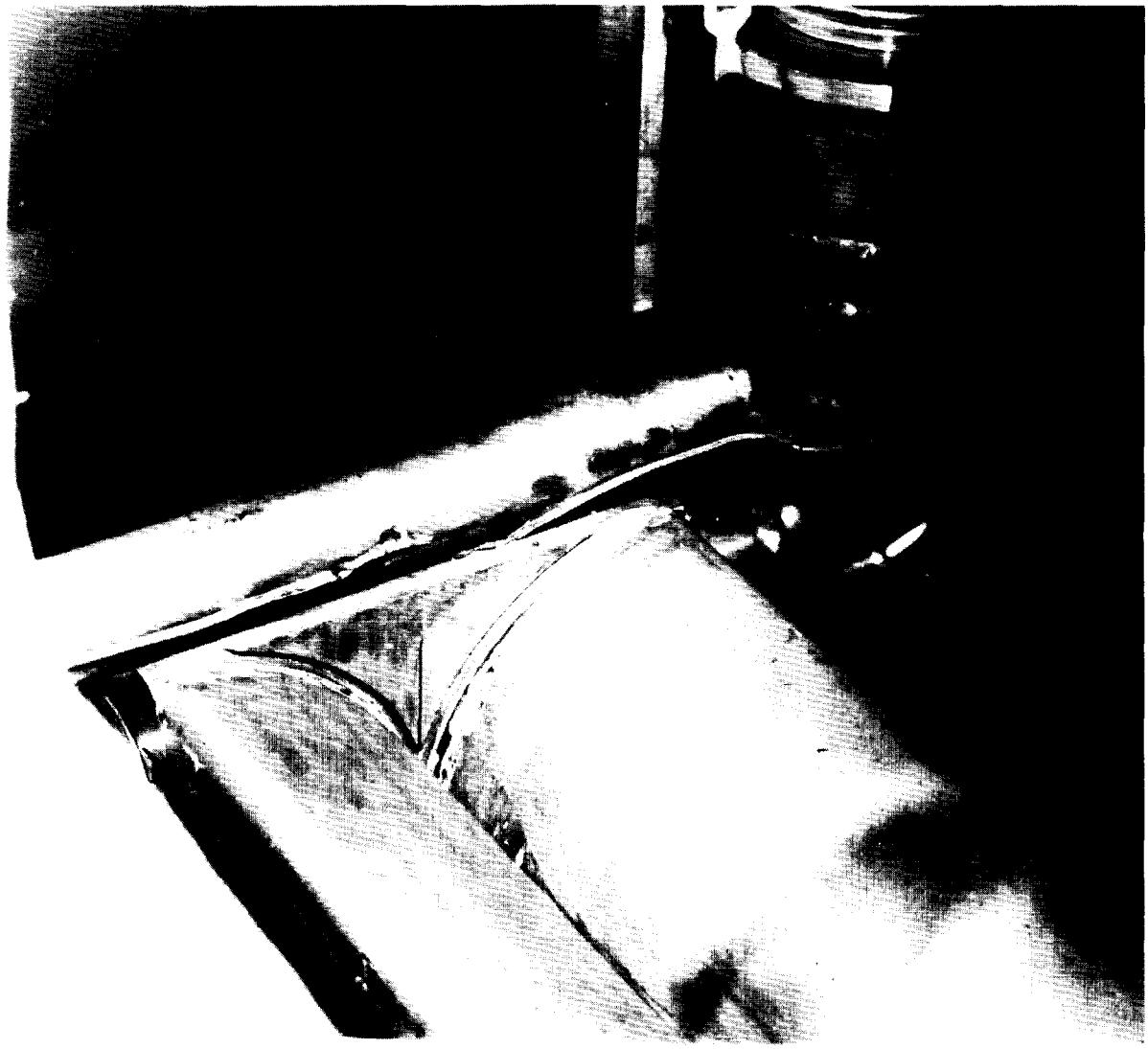

Fig.3b: Fractional energy dump. Two curved elements take a beam with a narrow line focus.

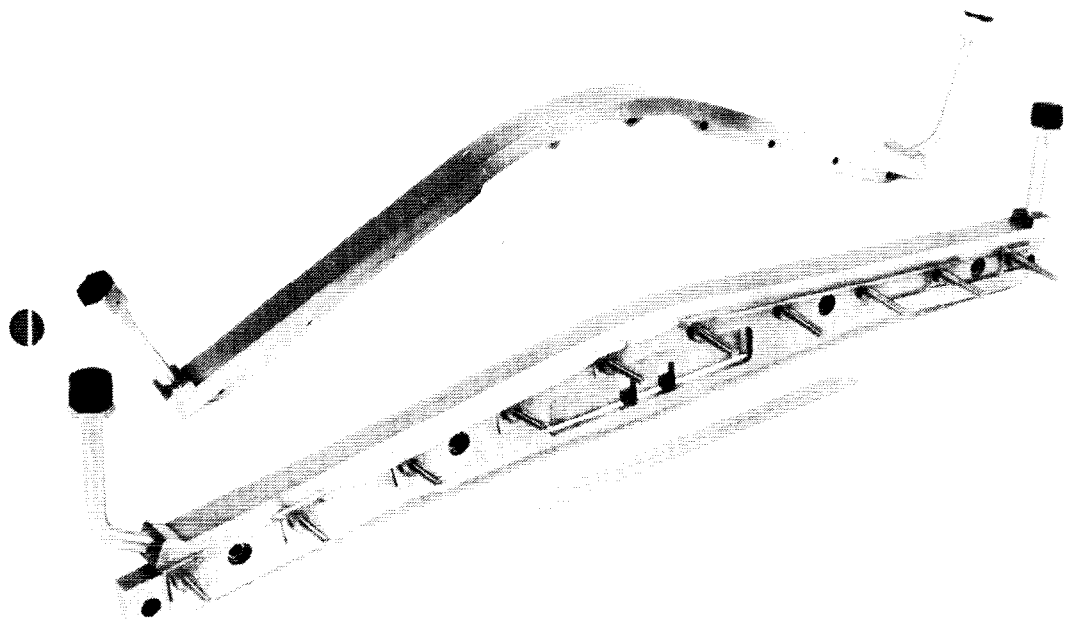

Fig.3c: Elements of the JET actively cooled divertor project. The elements are wedge shaped and mountred to a strong steel back.

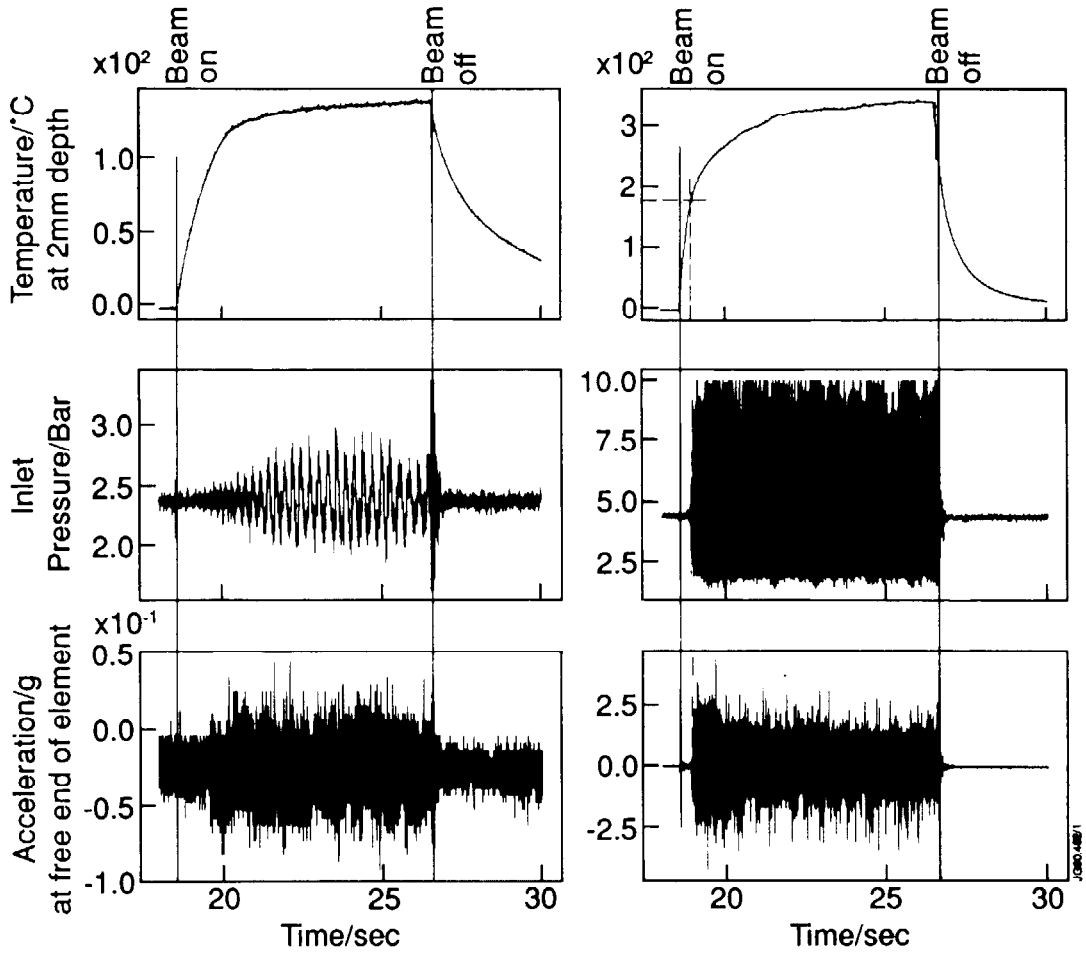

Fig. 5 a) Flow velocity: 0.7 m/s
Pressure: 2.35 bar
Power density: 5.7 MW/m²

b) Flow velocity: 3 m/s
Pressure: 4.5 bar
Power density: 13.75 MW/m²

Fig.4: Noise spikes observed on the water pressure signal for low flow velocity (left) and high velocity (right) At the low velocity we see a clear dominant frequency indicating vapotron action. At the high velocity the noise is white.

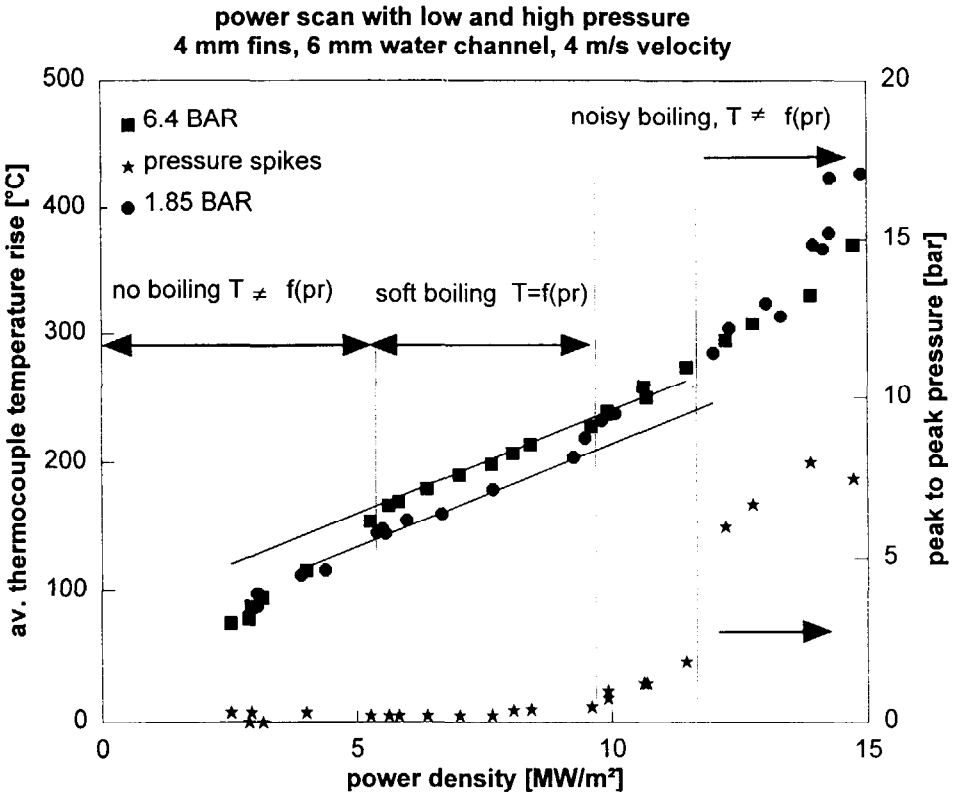

Fig.5: Vapotron body temperature 3 mm below the exposed surface versus power density. At low and high power density the heat transfer is independent of water pressure. In the intermediate range temperature increases with pressure. Pressure bursts are observed at high power densities.

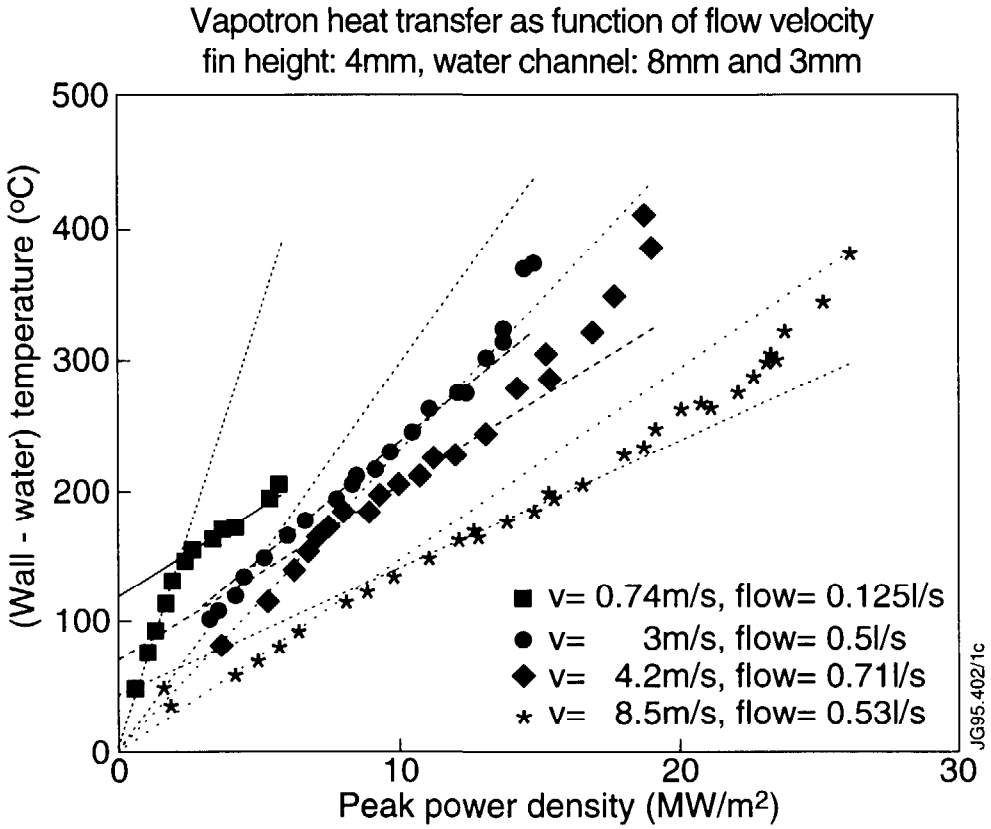

Fig.6: Temperature difference between the wall at the fin root and the bulk water for a vapotron with 4 mm high fins as a function of power density. At the onset of boiling the rate of temperature rise reduces. With increasing velocity the heat transfer improves before and after the onset of boiling. At the highest velocity the improvement with boiling is only marginal.

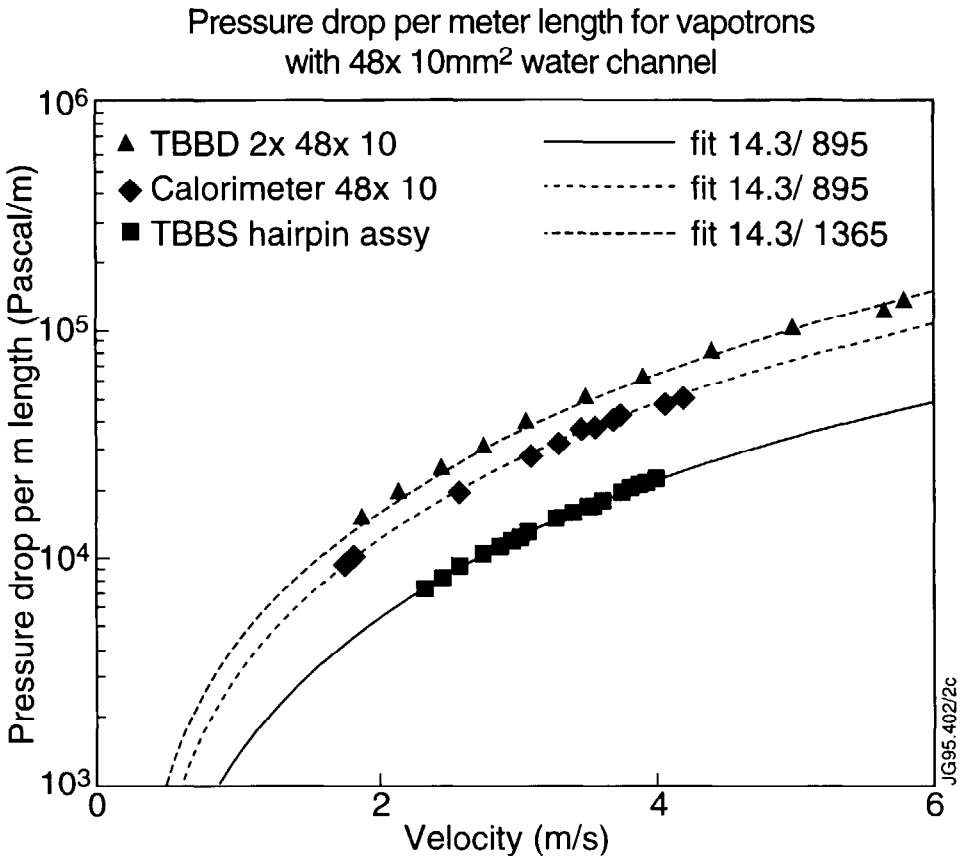

Fig.7: Pressure drop per metre length of the standard JET vapotron elements including feed/return loss. All elements have the cross section in Fig. 1. Test Bed Beam Dump and calorimeter are 1 m long. The scraper element is 500 mm long with hair pin flow. The pressure drop is described by the friction factors ξ_1 and ξ_2 in equation 4.

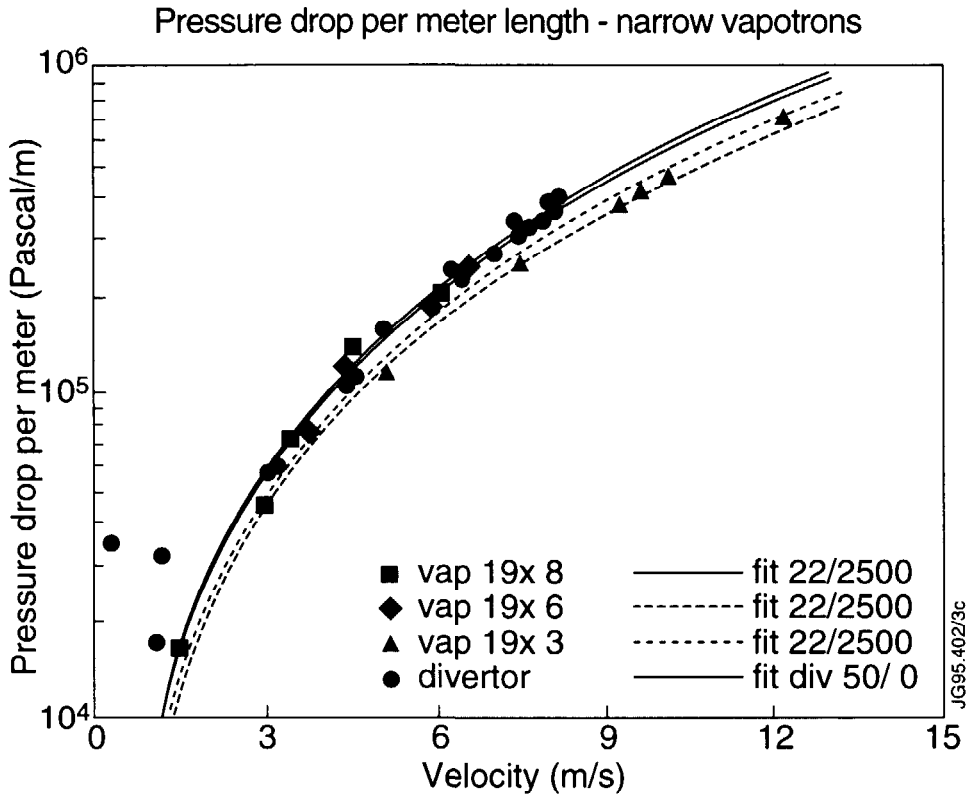

Fig.8: Pressure drop per metre length of the narrow vapotrons. All test sections are 485 mm long and the pressure drop is for 2 elements in series. The pressure drop of the divertor element is measured internally and extrapolated to 1 m length.

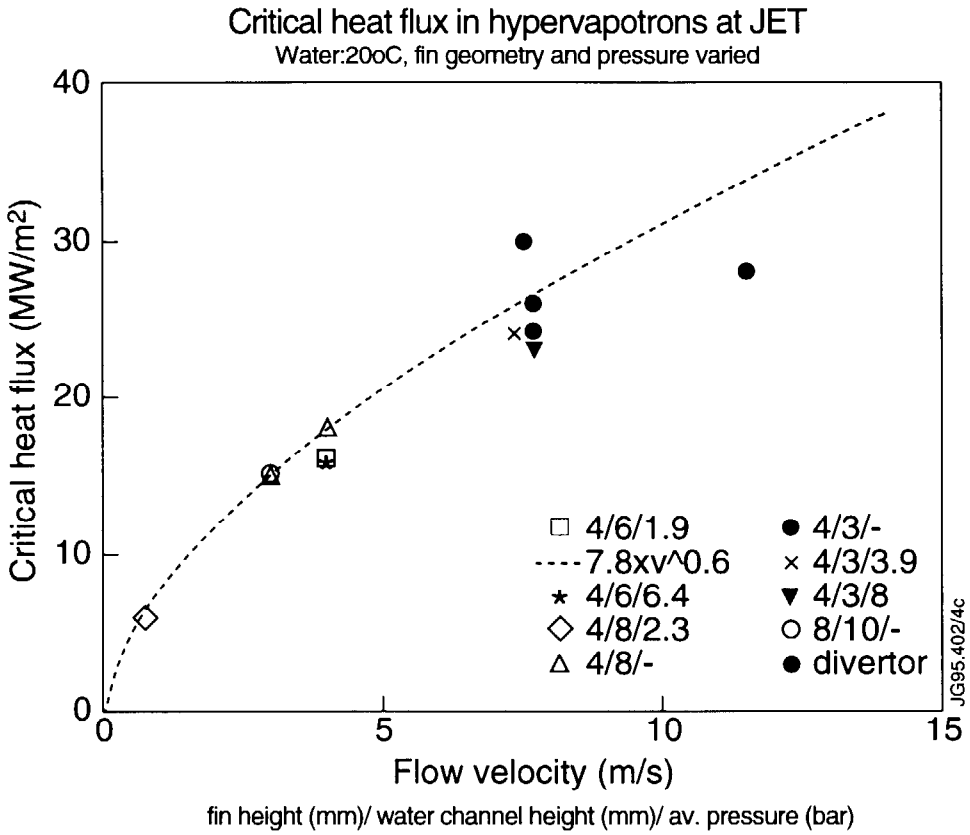

Fig.9: Critical heat flux as a function of bulk velocity. The symbols mark the energy at which the power scans were terminated. The fit is an upper limit to the measured points.

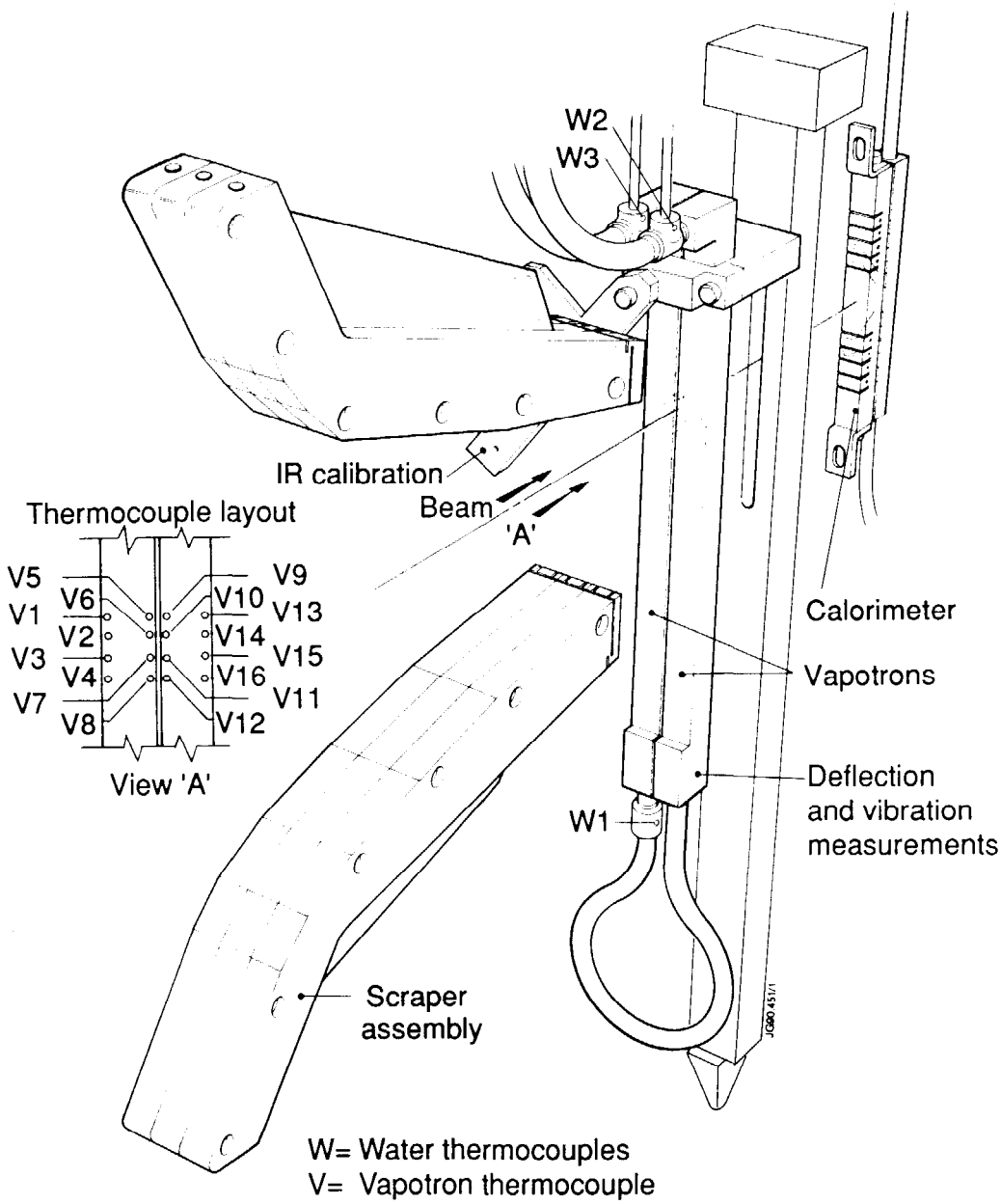

Fig.10: Schematic of the test rig used for the narrow vapotrons. The exposure is limited to 200 mm height by a scraper.

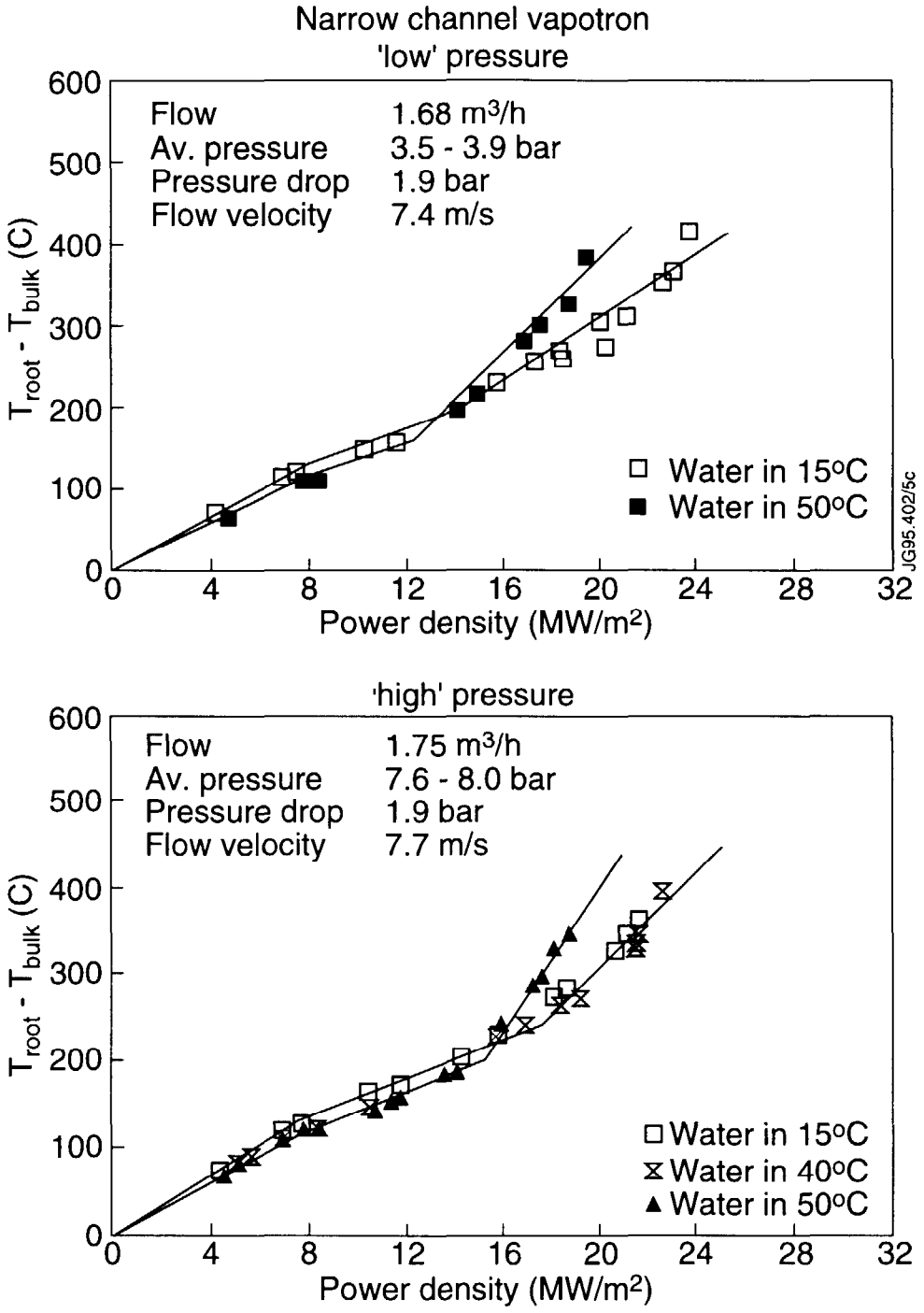

Fig.11: Power scans with varying water pressure and water temperature.

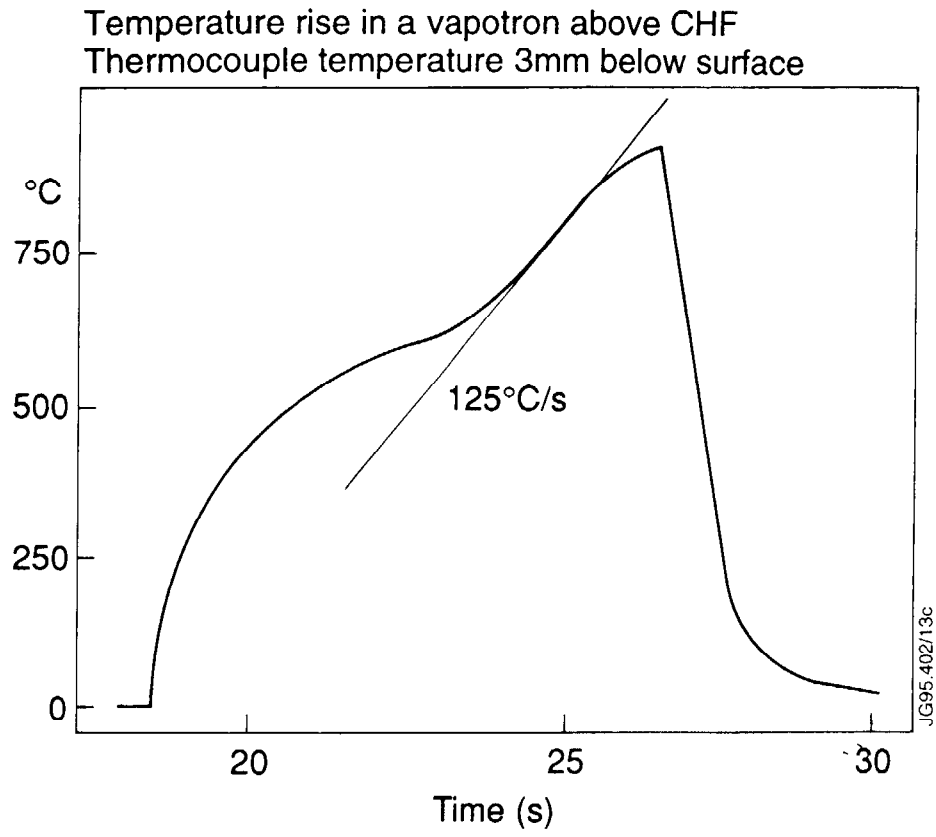

Fig.12: Temperature rise in the vapotron body 3 mm below the exposed surface above critical heat flux.

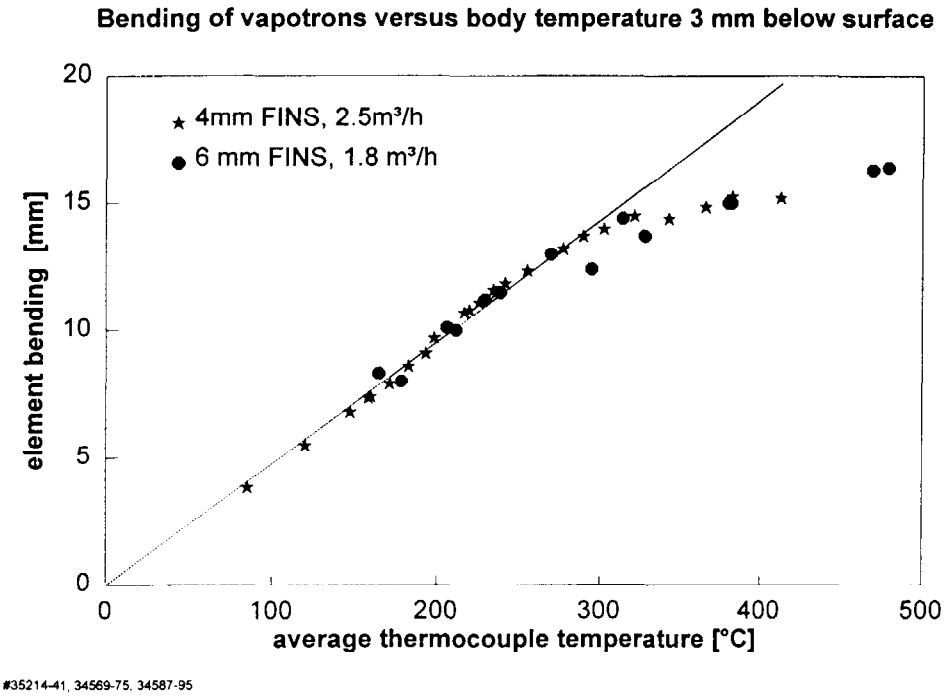

Fig.13: Bending of narrow vapotron elements. Bending is proportional to temperature up to 300 °C. Above 300 °C bending does not fully follow the temperture rise. This is an indication of plastic deformation.